Silicon (2022) 14:1629–1641
https://doi.org/10.1007/s12633-020-00938-9

ORIGINAL PAPER

Preparation of Zeolite 4A for Adsorptive Removal of Methylene Blue: Optimization, Kinetics, Isotherm, and Mechanism Study

Neway Belachew[1] · Hirpo Hinsene[1]

Received: 15 August 2020 / Accepted: 30 December 2020 / Published online: 4 February 2021

Abstract

In this study, we have reported a facile preparation of zeolite 4A from Ethiopia kaolin for the adsorptive removal of methylene blue (MB) dye. The formation of highly crystalline and pure phase zeolite 4A with cubic morphology was confirmed by powder X-ray diffraction (XRD) and scanning electron microscope (SEM) analysis. The efficiency of zeolite 4A for abatement of MB was investigated at varying adsorption parameters. Response surface methodology coupled with Box Behnken Design (RSM-BBD) was employed to optimize adsorption parameters. High regression ($R^2 = 0.9947$) and the low probability (p value <0.0001) values signify the validity of the quadratic model to predict the removal (%) of MB. The maximum MB removal (%) was 99.37% at the optimum combination of 50 mL of 10 mg/L of MB, 39.05 mg zeolite 4A, and 179.82 contact time (min). The adjusted R-square (R^2_{adj}) and standard deviations (SD) were validated the best fitting of pseudo-second-order kinetics and the Langmuir isotherm model for experimental values. The maximum adsorption capacity (Q_{max}) of zeolite 4A towards MB was found to be 44.35 mg g^{-1}. Electrostatic interaction, hydrogen bond, and n to π bond formation are predicted to be the plausible interaction mechanism of MB to the surface of zeolite 4A. The Fukui function and vibration analysis based on the density functional theory (DFT) further strengthened the proposed mechanism.

Keywords Zeolite 4A · Kaolin · Adsorption · Methylene blue · Box Behnken design

1 Introduction

Colored organic compounds discharged from different industries such as textiles, food, rubber, plastics, and paper, have taken a substantial contribution to the pollution environment. Such organic compounds show an adverse effect on the aquatic environment by decreasing the intensity of sunlight that reached the bottom [1]. Various colorants also behave as carcinogenic and mutagenic for aquatic lives [2]. Moreover, such organic compounds cause severe health problems, including, kidney dysfunction, brain, liver, central nervous, and reproductive system [3, 4]. Methylene blue is one of the commonest cationic dyes used in textile, chemical laboratories, staining cells in biology, medical science, and other dyeing industries [5, 6]. However, long-term exposure to MB can trigger serious health issues such as anemia, vomiting, nausea, and hypertension [7, 8]. Hence, it requires unwavering effort from the scientific community to introduce warranted techniques for the removal of dyestuffs from contaminated water. Photocatalysis [9], coagulation [10], membrane filtration [11], Fenton oxidation, biological treatment [12], and adsorption [13, 14] methods have been reported for abatement of dye from water. Among all, adsorption has taken the best alternative because it works in a simple operation set up and high efficiency [15, 16].

Activated carbon is the most widely used adsorbent material for the removal of dyes, but at the same time, it is expensive. Thus, searching for low-cost, sustainable sources and efficient adsorbents that substitute activated carbon is the prime concern in the field. Activated carbon from plant biomass [17, 18], Chitosan, and chitin [19, 20] from shrimp wastes, bentonite [21], and kaolin [22] clays have been reported as the low cost and highly efficient materials for the removal of dye. Kaolin is one of the most abundant and cheap clays widely utilized for numerous applications including the adsorption of water pollutants [23, 24]. It is mainly composed of kaolinite mineral which is a 1:1 aluminosilicate consisting of SiO_2 (46.5%), Al_2O_3 (39.5%), and H_2O (14%) [25].

✉ Neway Belachew
neway.du@gmail.com; neway@dbu.edu.et

[1] Department of Chemistry, Debre Berhan University, P.O.Box 445, Debre Berhan, Ethiopia

Despite this, kaolin owing to the low surface area, low surface porosity, and poor ion exchange capacity, is no longer used for efficient removal of dye [26, 27]. Hence, different modification techniques are employed to enhance the adsorption potential of kaolin such as surfactants capping [28], acid/base treatment [29], intercalation with Fe_3O_4 [30], mechanochemical [31], conversion to zeolitic materials [32]. Highly valuable zeolite materials from kaolin show a considerable interest due to hierarchical structure, high exchange capacity, environmental compatibility, and reasonable costs [33]. In this regard, there have been reported various zeolite types prepared from kaolin such as zeolite A [34], zeolite 4A [35], zeolite NaP [36], zeolite X [37], Zeolite Y [38], zeolite T [39], zeolite KA [40], zeolite N [41], ZSM-5 zeolite [42], and zeolite P [43]. The sources of kaolin from distinct regions and preparation methods are the causes for the formation of different types of zeolite. Zeolite 4A has been used as a water softening, a builder in detergents, separation, desiccant, catalysis, and adsorption applications [44, 45]. Due to these purposes, zeolite 4A has been prepared in excess than other types of zeolites [35]. The preparation of zeolite 4A from kaolin is carried out in a high-temperature activation of raw kaolin (metakaolinization) followed by reacted with NaOH in a hydrothermal vessel [46, 47]. In this technique, the formation of zeolite 4A is highly reliant on the calcination temperature [46, 48]. For the activation, a temperature ranging from 500 °C to 900 °C was reported in the literature [44, 45, 49]. However, the activation temperature for zeolite 4A preparation is strongly dependent on the composition and crystallinity of the raw kaolin [48].

Hence, this work aimed to attempt the preparation of zeolite 4A from local Ethiopian kaolin at different metakaolinization temperatures (600 °C to 800 °C). To the best of our knowledge, there is no report on the preparation of zeolitic materials from the Belesa kaolin, the southern part of Ethiopia. Moreover, the study focused on the characterizations and adsorptive removal of MB. Response surface methodology (RSM) coupled with Box Behnken design (BBD) was employed to optimize the adsorption efficiency of zeolite 4A. The plausible interaction mechanism of MB onto zeolite 4A was also investigated by computational analysis based on the Density Functional Theory (DFT).

2 Materials and Methods

2.1 Materials

The raw kaolin was collected from *Belesa* district, *Hadiya* Zone, Ethiopia (Fig. S1). Hydrochloric acid (HCl, 37%), sodium hydroxide (NaOH, 98%) pellets were procured from Alphax Chemical Industry (India). MB (molar weight of 319.8 g/mol and $\lambda_{max} = 664$ nm) with 99% purity was obtained from Sigma Aldrich. The rest of all chemicals used in this study were analytically graded. Deionized water was used throughout the whole experiment.

2.2 Preparation of Zeolite 4A from Kaolin

The raw kaolin was washed three times with distilled water to remove surface contaminants then dried with ceramic crucible at 100 °C for 1 h in the hot air oven. The dried kaolin was crushed to fine particles using mortar and pestle for further calcination process to get metakaolin. Specifically, 10 g of powdered kaolin in a different crucible was calcined at a temperature of 600 °C, 700 °C, and 800 °C each for 2 h. The samples were removed from the furnace and allowed to cool in vacuum desiccators. Then zeolite 4A was prepared from metakaolin by modifying the protocol reported elsewhere [33]. Herein, we have applied mild-hydrothermal conditions where the reaction takes place in a reflux setup. Specifically, 5 g of metakaolin was fused with 50 mL of 4 M NaOH solution. The mixture was transferred to a round—bottom flask for thermal treatment under reflux setup at 90 °C for 6 h. Finally, the filtrate was washed using distilled water to remove excess alkaline until the mixture became neutral. The as-prepared zeolite 4A was dried in the oven at 105 °C for 5 h then cooled in a vacuum desiccator.

2.3 Characterization Techniques

FTIR spectra were obtained from the pelletized of the powder sample mixed with KBr using a SHIMADZU-IR PRESTIGE-2 Spectrometer. The powder XRD patterns were recorded by PANalytical X'pert pro diffractometer at 0.02 degrees/s scan rate using Cu-kα 1 radiation (1.5406 Å, 45 kV, 40 mA) to investigate the crystal structure of raw kaolin and zeolite. The surface morphology was investigated by scanning electron microscopy (SEM) using a JEOL Electron Microscope operating at 15 kV. The surface charge of zeolite 4A was investigated using the pH of point zero of charge (pHzpc) analysis. Specifically, 50 mL of NaCl (0.1 M) solution was placed in a 100 mL flask. Then, the pH was adjusted with an initial value 2, 4, 6, 8, and 10 using either sodium hydroxide (0.1 mol/L) or hydrogen chloride (0.1 mol/L), and after that 0.15 g of zeolite 4A was added to each solution. After 24 h aging, the final pH of the solution was measured. The plot of changing pH (pH final - pH initial) against the pH of initials was used to predict the pH_{ZPC}.

2.4 Statistical Optimization of Adsorption Studies

The adsorption efficiency of zeolite 4A to MB was carried out in a batch adsorption mode. Explicitly, 50 mg of the zeolite 4A was added into 50 mL of MB solution (10–20 mg/L) and stir continuously to adsorption equilibrium. The pH of the

solution was adjusted using HCl (0.1 mol/L) and NaOH (0.1 mol/L). The % removal (Eq. 1) and adsorption capacity at a time, q_t (Eq. 2) of zeolite 4A towards MB were investigated by measuring the absorbance at $\lambda_{max} = 664$ nm. The statistical optimization of MB adsorption mainly focused on three independent factors (zeolite 4A dose (mg), contact time (min), and concentration of MB (mg L^{-1})). These three variables are selected because adsorption processes are highly reliant on them. The remaining variables including pH and room temperature (25 °C) were constant throughout the whole adsorption process. The statistical analysis was computed by the Design Expert 11 software. The levels of variables for RSM-BBD were based on Table 1.

$$\text{Removal}\ (\%) = (C_o - C_t)/C_o * 100 \quad (1)$$

$$q_t = (C_o - C_t)\ v/m \quad (2)$$

Where C_o is the initial concentration of MB (mg L^{-1}), C_t the concentration of MB (mg L^{-1}) at a time 't', m is the mass of the adsorbent and v is the volume of solution.

2.5 Adsorption Kinetics Models

The kinetics of MB adsorption was carried out at a fixed dose of adsorbent (50 mg), 100 mL of 50 mg L^{-1} of adsorbate, and pH 8. Pseudo-first order (Eq. 3), pseudo-second order (Eq. 4) and intraparticle diffusion (Eq. 5) kinetic models were employed for fitting the kinetic data.

$$q_t = q_e \left(1 - exp^{(-k_1 t)}\right) \quad (3)$$

$$q_t = \frac{k_2 q_e^2 t}{k_2 q_e t + 1} \quad (4)$$

$$q_t = C + \left(k_{id}\ t^{\frac{1}{2}}\right) \quad (5)$$

Where k_1 (min^{-1}), k_2 (g mg^{-1} min^{-1}), and k_{id} (mg g^{-1} $min^{-1/2}$) are the rate constants for pseudo-first order, pseudo-second order, and interparticle diffusion models respectively. q_t and q_e in mg g^{-1}, are the theoretical adsorption capacity at a time (t) and equilibrium time respectively. C (mg g^{-1}) is a constant related to the thickness of the boundary layer.

2.6 Adsorption Isotherms Models

The adsorption isotherm studies were performed for 180 min contact time by taking 50 mg of adsorbent and 100 mL of various concentrations of MB ranging from 10 mg L^{-1} to 50 mg L^{-1} at pH 8. The Langmuir (Eq. 6), Freundlich (Eq. 7), and Liu (Eq. 8) adsorption models were used to investigate the equilibrium data.

$$q_e = \frac{Q_{max}\ K_L\ C_e}{1 + K_L\ C_e} \quad (6)$$

$$q_e = K_F\ C_e^{1/n_F} \quad (7)$$

$$q_e = \frac{Q_{max}\ (K_g\ C_e)^{n_L}}{1 + (K_g\ C_e)^{n_L}} \quad (8)$$

where q_e (mg g^{-1}) and c_e (mg L^{-1}) are equilibrium adsorption capacity of adsorbent and the residual concentration of MB at equilibrium, respectively; Q_{max} is the maximum adsorption of the adsorbent (mg g^{-1}); K_L (Lmg^{-1}), K_F (mg g^{-1} (mg L^{-1})$^{-1/nF}$) and Kg (L mg^{-1}) are the equilibrium constants for Langmuir, Freundlich, and Liu isotherm models, respectively; n_F and n_L are the dimensionless exponents for Freundlich, and Liu isotherm models, respectively.

The degree of fitness of the kinetics and equilibrium data towards the nonlinear curves of the models were validated by determination of R-square, R^2 (Eq. 9), the adjusted R-square, R^2_{adj} (Eq. 10), and the standard deviation of residues, SD (Eq. 11).

$$R^2 = \frac{\sum_i^n \left(q_{i,exp} - q\text{exp}\right)^2 - \sum_i^n \left(q_{i,exp} - q_{i,model}\right)^2}{\sum_i^n \left(q_{i,exp} - q\text{exp}\right)^2} \quad (9)$$

$$R^2_{adj} = 1 - \left(1 - R^2\right)\left(\frac{n-1}{n-p-1}\right) \quad (10)$$

$$SD = \sqrt{\left(\frac{1}{n-p}\right) \sum_i^n \left(q_{i,exp} - q_{i,model}\right)2} \quad (11)$$

where $q_{i,exp}$ is adsorption capacity at a particular experimental; q_{exp} is the average of all experimental q values; $q_{i,\ model}$ is individual theoretical q value predicted by the model; p is the number of parameters in the fitting model, and n is the number of experiments.

Table 1 The experimental levels of factors used for RSM-BBD

Factors	Levels		
	Low (−1.000)	Center (0.000)	High (1.000)
A=x_1: Contact time (min)	30	105	180
B=x_2: Adsorbent dose(mg)	20	40	60
C=x_3: MB concentration (mg/L)	10	15	20

3 Results and Discussions

3.1 Characterizations of Zeolite 4A

The powder XRD patterns of kaolin and zeolitic material prepared at different calcination temperatures are presented in Fig. 1. The XRD phase identification of raw Ethiopian kaolin (Fig. 2a) was found to be best fitted to kaolinite (COD: 00–900-9230, Fig. S2) mineral [50]. Figure 2 b-c, show the diffractograms of zeolitic materials obtained from different temperatures. The zeolitic material prepared at 600 °C calcination shows the formation of zeolite 4A with excess quartz (Q) as an impurity. Whereas pure zeolite 4A (JCPDS 43–0142) [51] was prepared at 700 °C and 800 °C (Fig. 2c and d). Hence, metakaolin prepared from at 700 °C calcination, due to an economic point of view, is recommended for the preparation of zeolite 4A. Zeolite 4A has the diffraction peak at 2 θ = 10.14°, 12.44°, 16.08°, 21.66°, 23.98°, 27.1°, 29.94°, and 34.2° [51].

The FTIR spectra of raw kaolin and zeolite 4A are shown in Fig. 2. The raw kaolin (Fig. 2a) shows the presence of a well-identified peak at 3692, 3669, 3652 cm^{-1}, and 3620 cm^{-1} due to O-H stretching is attributed to the highly ordered structure of the raw kaolin [52]. The vibrational peaks observed at 1020 cm^{-1} and 921 cm^{-1} are due to Si-O-Si and Al-OH stretching vibration, respectively [53]. Moreover, additional peaks at 712, 692, 528 cm^{-1} could be assigned to Si-O-Al bending peaks. While Zeolite 4A (Fig. 2b) shows the broad peak at around 3435 cm^{-1} due to the O-H stretching of water and O–H groups on the zeolite 4A surface [54]. The O-H group bending vibration is located at 1660 cm^{-1}. The characteristic strong band of zeolite 4A at 999 cm^{-1} can be assigned to stretching vibration of Si–O and Al–O groups [54]. The

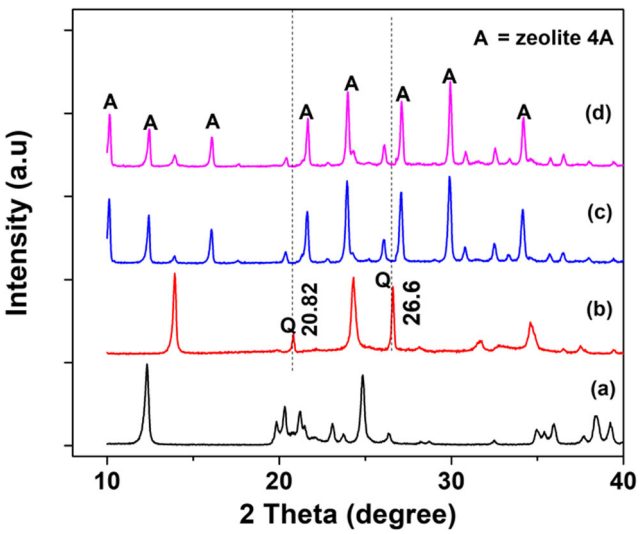

Fig. 1 The powder XRD patterns of (**a**) raw kaolin, (**b**), (**c**), and (**d**) zeolite materials prepared at 600 °C, 700 °C, and 800 °C calcination temperatures, respectively

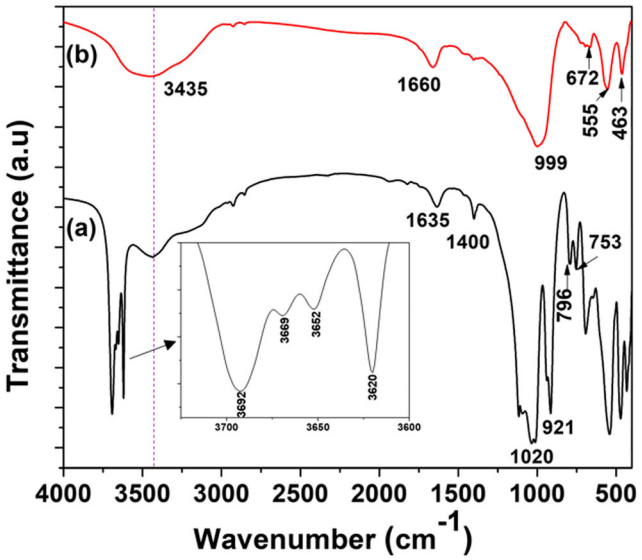

Fig. 2 FTIR spectra of (**a**) raw kaolin (**b**) zeolite-4A prepared from kaolin

peaks observed at 672 cm^{-1} and 555 cm^{-1} can be attributed to vibration modes of the zeolite framework [51]. The peak located at 463 cm^{-1} relates to the bending vibration of Si-O or Al-O groups in the zeolite structure [55].

SEM images were captured to investigate the surface morphology of zeolite 4A. Figure 3 shows the SEM images zeolite 4A obtained from different magnification scale. The image demonstrates the formation of a well crystallized zeolite 4A with cubic morphology. The shape agrees with the zeolite 4A reported by Dahani et al. [56] stating that zeolite 4A from kaolin has cubic morphology. The average sizes of cube diameters were found to be 1.16 μm.

3.2 Adsorption Studies

3.2.1 Point of Zero Charges (pH_{pzc}) and Effect of pH of the Solution

The pH value of the solution has an important role that causes a change in the surface charge of the adsorbent. The hydronium (H_3O^+) and hydroxyl (OH^-) ions absorbed on the adsorbent surface are responsible for the adsorption through electrostatic interaction. Hence, the behavior surface charge is explained based on the pH_{pzc}. As it is shown in Fig. 4a, the adsorbent surface became positively charged at the pH < pH_{pzc} (pH = 6.86) due to the protonation of the carboxyl. Under these conditions, the anionic dye preferentially adsorbed onto zeolite 4A. Whereas, the pH > pH_{PZC}, the surface became negative due to hydroxylation of the zeolite surface which in turn suitable for adsorption of the cationic dye. Thus, the maximum removal of MB, a cationic dye, is expected at the high pH of the solution. The removal (%) of MB at varying initial pH is presented in Fig. 4b. More than 90% maximum removal was obtained at pH = 8–10, and at the

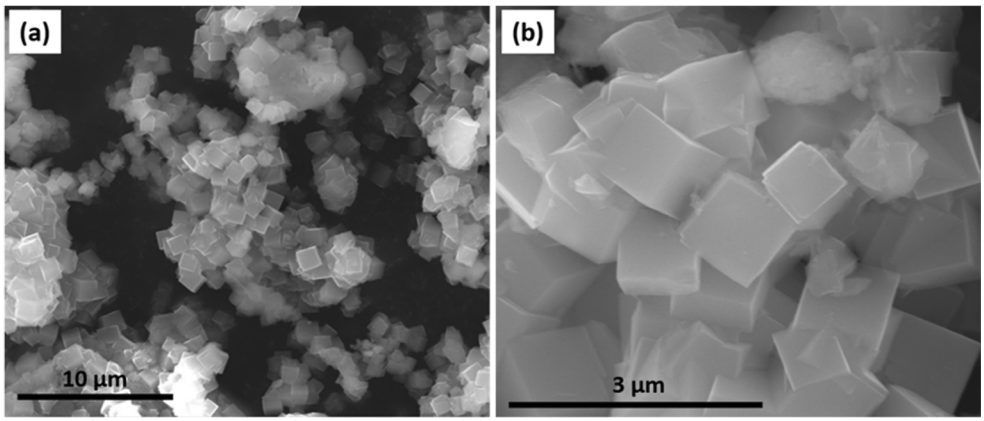

Fig. 3 The representative SEM images of zeolite 4A at different magnification scale

same time, poor adsorption efficiency is obtained at pH <6. value. A similar analogy was reported by literature [8].

3.2.2 Statistical Optimizations of MB Adsorption

Optimizations of the adsorption variables using statistical approaches are crucial for saving time and resources. Moreover, the statistical analysis gives clear information about the adsorption variables and minimizes the experimental errors. Herein, the BBD statistical approach coupled with RSM was used to optimize the adsorption of MB into zeolite 4A. BBD is second-order designs (Eq. 12) based on three-level factorial designs [57]. The complete BBD matrix for the three important factors [contact time (A), zeolite 4A (B) dose, and MB concentration (C)] and response [Removal (%)] both the coded and real values are presented in Table 2.

$$Y = b_0 + \sum_{i=1}^{n} b_i X_i + \sum_{i=1}^{n} b_{ii} X_i^2 + \sum_{i=1}^{n-1} \sum_{j=i+1}^{n} b_{ij} X_i X_j \qquad (12)$$

where Y is the predicted response (Removal (%)) of MB, b is a constant while, b_i, b_{ii}, and b_{ij} refers to the linear, quadratic, and interaction coefficients, respectively. X_i and X_j are lists of the coded values of factors.

The empirical relationship between adsorption variables and MB removal (%) efficiency generated from the BBD was found to be as it is shown in Eq. 13.

$$\begin{aligned} \textbf{Removal}\ (\mathbf{Y}) = {} & +73.72 + 17.8\ \mathrm{A} \\ & +10.4125\ \mathrm{B} - 5.6125\ \mathrm{C} \\ & +0.7500\ \mathrm{AB} - 3.20\ \mathrm{AC} - 0.9250\ \mathrm{BC} - 6.10\ \mathrm{A2} - 2.27\ \mathrm{B2} \\ & +5.83 \end{aligned} \qquad (13)$$

Where the positive coefficients of factors show their role in enhancing the adsorption removal (%) of MB and vice versa. The statistical parameters from ANOVA are summarized in Table 3. The F-Value (145.03) shows the significance of the quadratic model to sufficiently explain the adsorption of MB with only a 0.01% chance that an F-value larger than this due to noise. The *p* value (<0.0001) further confirms the significance of the model. Moreover, the linear (A, B, and C) and quadratic (AC, A^2, B^2, and C^2) terms of the quadratic equation (Eq. 13) were significant (p value <0.05) in the 95% confidence level. *P* values greater than 0.1000 indicate the model terms are not significant, and therefore AB and BC interaction terms are

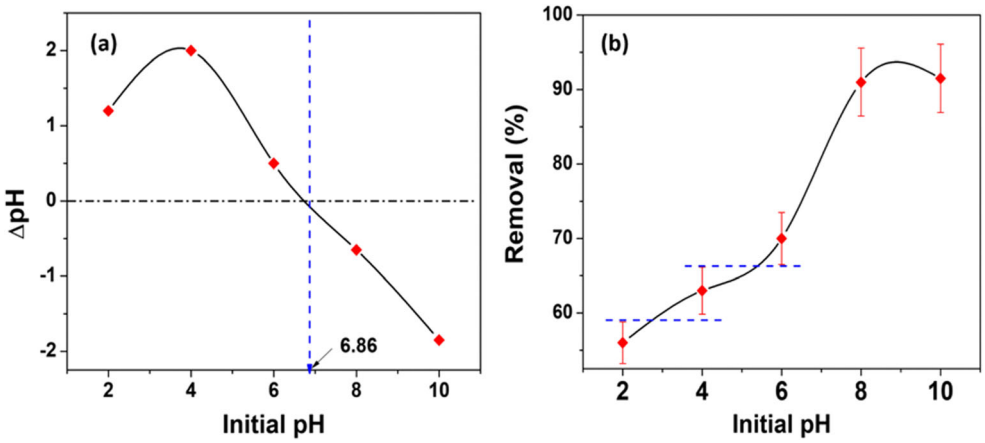

Fig. 4 (**a**) the point of zero charges of zeolite, (**b**) the removal (%) of MB at varying pH (with 5% error bar)

Table 2 The RSM-BBD design matrix of the three variables with coded and real values; and Response with actual and predicted

Run Order	Coded Values			Real Values			Response	
	Contact time	Adsorbent dose	Concentration	Contact time	Adsorbent dose	Concentration	Actual Value	Predicted Value
1	−1.000	1.000	0.000	30	60	15	57.40	57.21
2	0.000	0.000	0.000	105	40	15	71.50	73.72
3	0.000	−1.000	1.000	105	20	20	61.50	62.18
4	0.000	0.000	0.000	105	40	15	75.50	73.72
5	−1.000	0.000	−1.000	30	40	10	57.20	58.06
6	−1.000	−1.000	0.000	30	20	15	37.40	37.89
7	1.000	0.000	1.000	180	40	20	83.30	82.44
8	1.000	0.000	−1.000	180	40	10	99.00	100.16
9	0.000	1.000	1.000	105	60	20	79.80	81.15
10	0.000	0.000	0.000	105	40	15	72.90	73.72
11	1.000	1.000	0.000	180	60	15	94.80	94.31
12	0.000	−1.000	−1.000	105	20	10	72.90	71.55
13	−1.000	0.000	1.000	30	40	20	54.50	53.34
14	0.000	0.000	0.000	105	40	15	73.20	73.72
15	0.000	1.000	−1.000	105	60	10	94.90	94.23
16	1.000	−1.000	0.000	180	20	15	71.80	71.99
17	0.000	0.000	0.000	105	40	15	75.50	73.72

not significant. There is also a 47.39% chance that a Lack of Fit F-value larger this due to noise. Model validation further investigated using regression (R^2) analysis. The Predicted R^2 (0.9584) is in reasonable agreement with the Adjusted R^2 (0.9878) because their difference is less than 0.2. This implies that the quadratic model (Eq. 4) is adequate to explain the interaction between factors and removal (%) of MB.

Figure 5 shows the diagnostic plots that give further information about the validation of model adequacy. The plot of predicted and actual removal (%) of MB (Fig. 5a) shows data are well fitted to the linear regression. This is shown that the model adequately explains the experimental range. Figure 5b shows the plot of normal % probability against externally studentized residuals also known as the normal plot of

Table 3 The ANOVA analysis of MB adsorption based on the Quadratic model

Source	Sum of Squares	df	Mean Square	F-value	p value	Fit Statistics	
Model	4009.12	9	445.46	145.03	< 0.0001	SD=1.75	
Residual	21.50	7	3.07	–	–	CV(%)=2.42	
Lack of Fit	9.29	3	3.10	1.01	0.4739	R^2=0.9947 Predicted R^2=0.9584	
Pure Error	12.21	4	3.05	–	–	Adjusted R^2=0.9878	
Terms	Coefficients			SE Coefficients	Mean Square	F-value	p value
Constant	73.72			0.7838	–	–	–
A	17.80			0.6196	445.46	825.24	< 0.0001
B	10.41			0.6196	2534.72	282.39	< 0.0001
C	−5.61			0.6196	867.36	82.05	< 0.0001
AB	0.7500			0.8763	252.00	0.7325	0.4204
AC	−3.25			0.8763	2.25	13.76	0.0076
BC	−0.9250			0.8763	42.25	1.11	0.3262
A^2	−6.07			0.8541	3.42	50.55	0.0002
B^2	−2.30			0.8541	155.26	7.24	0.0311
C^2	5.85			0.8541	22.23	46.95	0.0002

residuals. Basically, the studentized residuals are useful for detecting the outliers. The arrangement of points on this graph (Fig. 5b) is linear, which designates the adequacy of the model and the normal distribution of errors across all runs. Figure 5c demonstrates a plot of externally studentized residual versus the run number, that conducts a t-test for each residual. The points dropping outside the red limits are considered as outliers. Therefore, all the points in Fig. 5c within the range of the model assumptions and there are no outliers observed. The comparative effect of all the adsorption factors at a particular point in the design space is obtained from the perturbation plot (Fig. 5d). The perturbation plot helps to identify the factor that most influences the removal (%) of MB dye. The steepest slope for factor A (slope = 17.8) than B (10.4125) and C (− 5.6125) shows that MB removal (%) is sensitive to contact time. Relatively, the flat line for factor "C" shows minimal dependence of MB removal on this factor.

The 3D surface plot of the adsorption process helps to visualize the interaction between factors for the removal (%) MB. Figure 6 shows the 3D surface plots of MB adsorptive removal (%) at varying contact time (min), zeolite 4A (mg), and MB concentration (mg/L). As it is shown in Fig. 6a, the MB removal (%) increased with an increase in both zeolite 4A dose and contact time at a constant concentration of MB. While Fig. 6b shows, at constant zeolite 4A dose, the removal (%) increased when the adsorption time increased and the concentration of MB decreased. On the other hand, Fig. 6c shows an increased MB removal (%) was observed as the zeolite dose increase and MB concentrations decreased at a fixed contact time.

Generally, statistical optimization of the adsorption process aims to achieve the desired goal such as maximize, minimize, within the range, target, and none for the responses and factors [58, 59]. Herein, numerical optimization was desired to maximize removal (%) and factor values within the range. For example, Fig. 7 shows the maximum desirability ramp for the optimum combination of contact time (30–180 min), zeolite dose (20–60 mg), and MB concentrations (10–20 mg/L) to get maximum adsorption efficiency. Thus, the maximum adsorptive removal of MB was found to be 99.37% at the optimum combination of 10 mg/L of MB, 39.05 mg zeolite 4A, and 179.82 contact time (min).

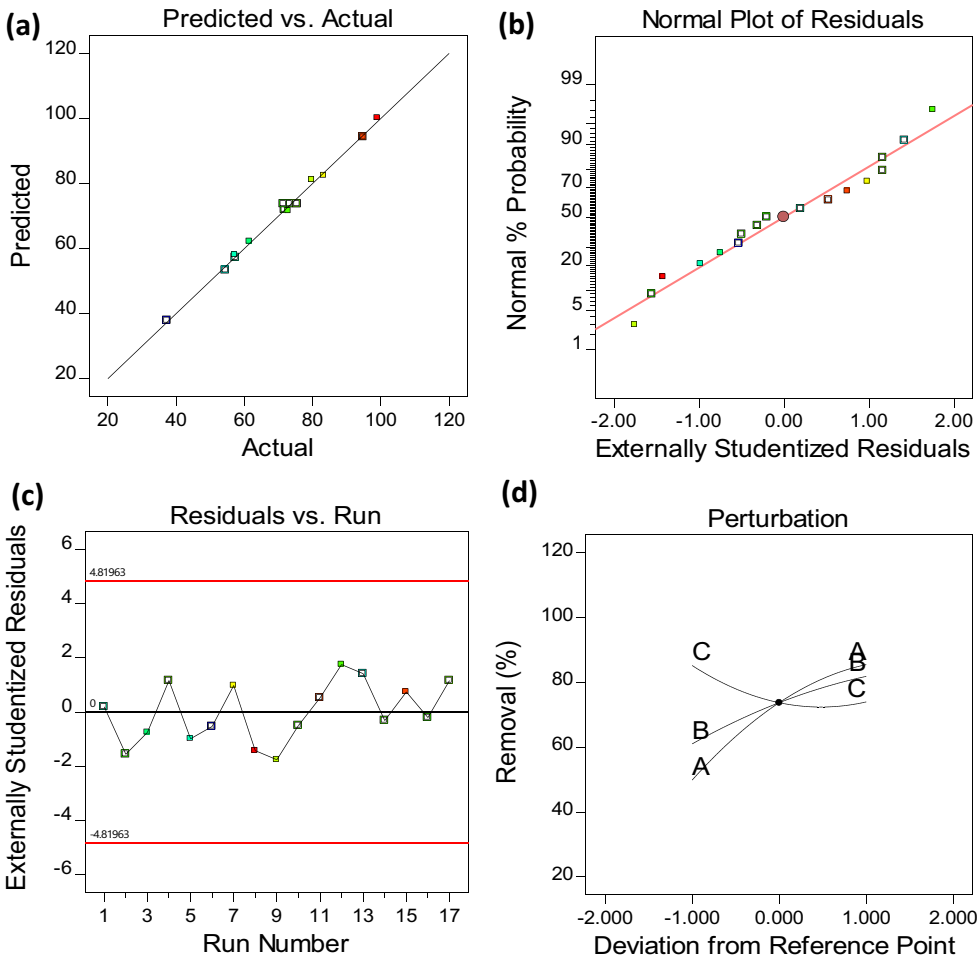

Fig. 5 The diagnostics curves of (**a**) predicted vs. actual of on the removal of MB, (**b**) the normal plot of residuals (**c**) the residual vs. run, and (**d**) perturbation of factors

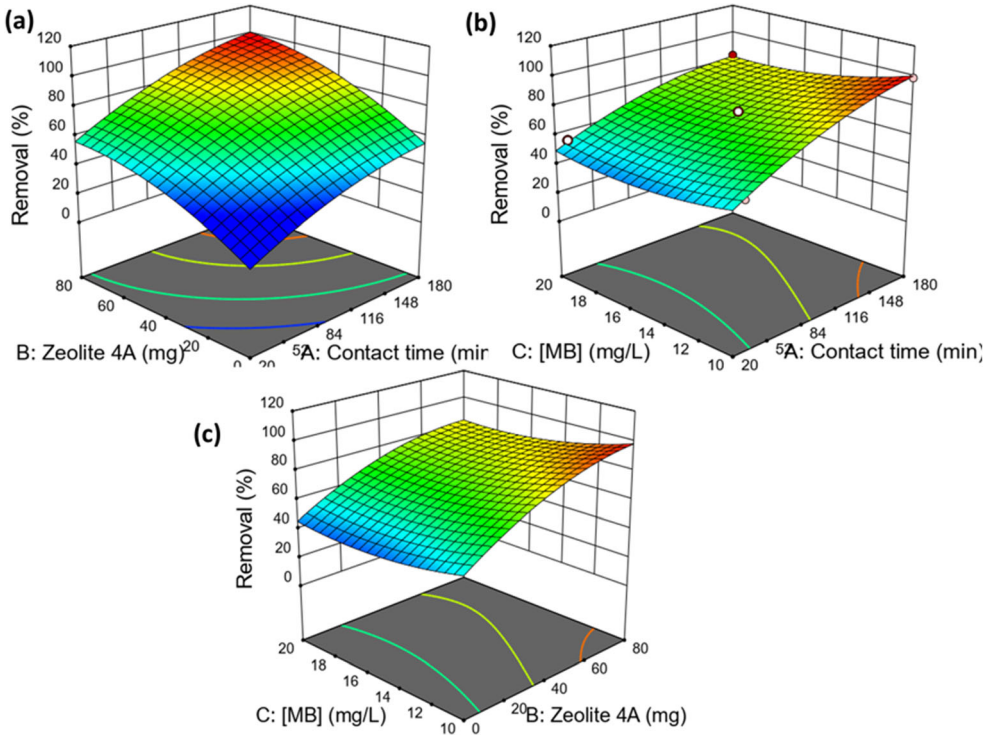

Fig. 6 The 3D surface plots for the removal of MB at different factors (**a**) the zeolite dose and contact time, (**b**) the initial MB concentration and contact time, and (**c**) the MB initial concentration and zeolite dose

3.2.3 Adsorption Kinetics Analysis

The nonlinear form of pseudo-first order, pseudo-second-order, and intraparticle diffusion models were used to assess the kinetics of MB adsorption onto zeolite 4A. The nonlinear kinetic curves and kinetic parameters are presented in Fig. 8 and Table 4, respectively. The statistical parameters, SD and R^2_{adj}, were used to evaluate the fitting of the kinetic data. The close agreement between the experimental value and model-predicted value was recognized by a lower SD and higher R^2_{adj} value [60]. As it is shown in Table 4, the pseudo-second-order kinetic model exhibits the lowest SD (0.7491 mg g^{-1}) and R^2_{adj} (0.99). This implies the adsorption capacity at a time t (q_t) obtained from the experiment shows a good agreement with the model value. Moreover, the adsorption equilibrium time can be derived from the best fitted kinetic model at t_{95} (min), the time when 95% of the absorbent saturation. The pseudo-second-order, best-fitted model, predicts 252.08 min equilibrium time is required to attain 95% (43.93 mg g^{-1}) saturation. However, the adsorption capacity obtained at 120 min, 150 min, and 180 min is 41.64 mg g^{-1}, 42.48 mg g^{-1}, and 43.065 mg g^{-1}, respectively, are comparable results to t_{95} (min). The adsorption capacity value at 252.08 min and 180 min shows only a decimal point variation and therefore 180 min could be considered as the equilibrium time. Fifty percent saturation of adsorbent surface can also be investigated from the t_{50} (min) value. As it is shown in Table 4, t_{50} (min) = 13.26 which indicates the fast adsorption

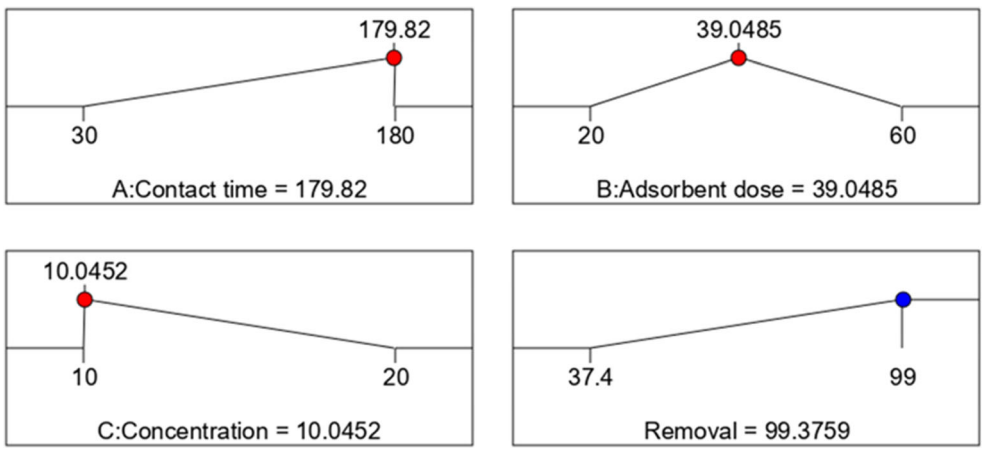

Fig. 7 The desirability ramp for optimization of three factors (contact time, zeolite 4A dose, and MB concentration) for the maximum degradation (%) of MB

Table 4 The parameters of Pseudo-first-order, Pseudo-second-order, and interparticle diffusion kinetic models

Pseudo first-order parameters	Pseudo second-order parameters	Interparticle diffusion parameters
k_1 (min^{-1})=0.05	k_2 (g mg^{-1} min^{-1})=0.0016	k_{id} (mg g^{-1} $min^{-1/2}$)=2.98
q_e (mg g^{-1})=41.57	q_e (mg g^{-1})=46.24	C (mg g^{-1})=9.34
R^2_{adj}=0.98	R^2_{adj}=0.99	R^2_{adj}=0.81
SD (mg g^{-1})=1.7701	SD (mg g^{-1})=0.7491	SD (mg g^{-1})=6.2235
t_{50}(min)=13.86	t_{50}(min)=13.26	–
t_{95} (min)=59.93	t_{95} (min)=252.08	–

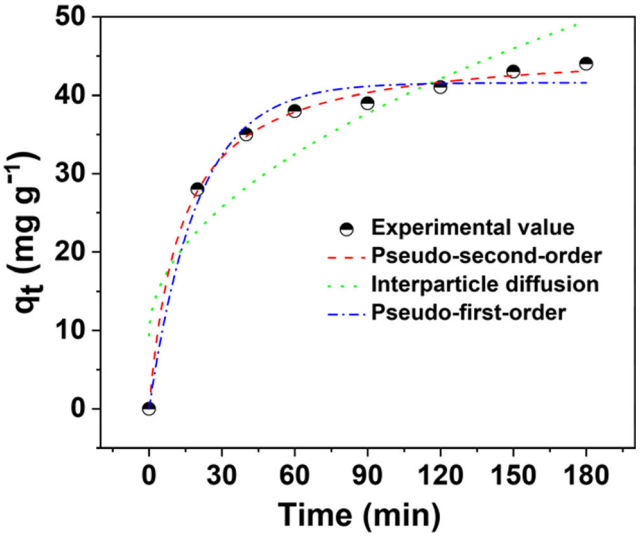

Fig. 8 The kinetics plots of MB adsorption onto zeolite 4A at 50 mg adsorbent, pH 4, and 50 mg L^{-1} MB

process takes place in the first 13 min for attaining 50% saturation.

3.2.4 Adsorption Isotherm Analysis

Langmuir, Freundlich, and Liu [60] adsorption isotherm models were applied to investigate the equilibrium phenomena. The nonlinear curves and parameters of the adsorption models are depicted in Fig. 9 and Table, respectively. One hundred milliliters of various concentrations of MB (10 mg L^{-1} to 50 m L^{-1}) at a fixed dose of zeolite 4A (50 mg), pH = 8, room temperature (25 °C) for 180 min (equilibrium time) contact time were employed to investigate the adsorption isotherm. R^2_{adj} and SD statistical parameters were also used to investigate the best fitting curve to the equilibrium adsorption data. The Langmuir model owing to the highest R^2_{adj} value (0.94) and minimum SD value (2.5088 mg g^{-1}) than Freundlich and Liu (Table 5) is recommended for investigating the equilibrium process. The maximum sorption capacity (Q_{max}) predicted based on the Langmuir model is 44.35 mg g^{-1}.

3.3 Plausible Adsorption Mechanism

Figure 10 shows the plausible adsorption mechanism of MB onto the zeolite 4A surface. The adsorption of MB can proceed via electrostatic interaction, hydrogen bonding, or n to π (coordinative covalent bonds) between the zeolite surface and MB dye [61]. The zeolite surface at pH > pH_{PZC} (6.86) becomes a negative (Si—O^-) where an electrostatic interaction takes place between the cationic MB through N^+ atom. The hydrogen bond between the silanol (Si-O-H) group of zeolites with N-atom of MB (Fig. 10) is another possible interaction that helps for the adsorption process. Besides, the n to π is an alternative interaction between ionic charge (Si-O^-) of zeolite surface and an empty orbital of S atom in the aromatic structure of MB. The lone pair electron from oxygen atom transfer to S atom is used to make coordinate covalent bonds. The adsorption mechanism of MB onto zeolite 4A was further investigated by the first principle analysis. Herein, the density functional theory (DFT) was employed to optimize and frequency analysis of MB, representative zeolite structure, and zeolite-MB using the Gaussian 09 software. The B3LYP functional with a 6–31 g* a basis set was used to compute the structure. The Fukui function analysis [62, 63] was also used to investigate the local reactivity sites of MB. Figure 11 shows

Table 5 The adsorption isotherm parameters of Langmuir, Freundlich and Liu models

Langmuir parameters	Freundlich parameters	Liu parameters
Q_{max} (mg g^{-1})=44.35	K_F (mg g^{-1} (mgL^{-1})$^{-1/nF}$)=30.23	Q_{max} (mg g^{-1})=42.99
K_L (L mg^{-1})=2.71	n_F=7.54	K_g (L mg^{-1})=2.61
R^2adj=0.94	R^2adj=0.75	*n*=1.41
SD (mg g^{-1})=2.5088	SD (mg g^{-1})=4.5536	R^2adj=0.92
		SD (mg g^{-1})=2.6332

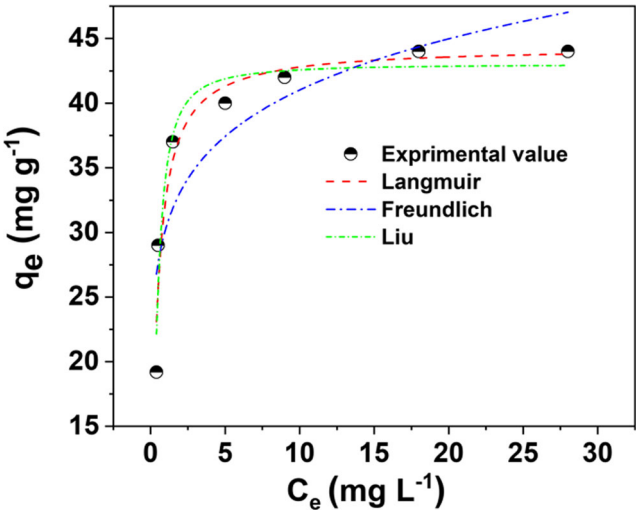

Fig. 9 The equilibrium isotherm plots of MB adsorption onto zeolite 4A at pH 8, 50 mg adsorbent, and 180 min contact time

the frontier molecular orbitals (MO), highest occupied MO (HOMO) and lowest unoccupied MO (LUMO) energy gap (ΔE) of MB. As shown in Fig. 11, an electron acceptor center or LUMO of MB resides on S atoms and this implies that electron zeolite surface (Si-O$^-$) can make a dative bond to S atom of MB. Whereas, the HOMO of MB is a nucleophilic center that is shown that the N atom is responsible for the formation of H bonding to the silanol group of zeolite surface. The Fukui function, f(r) (Eq. 14) gives numerical information about the reactivity of an atom in a molecule, especially the frontiers MOs based on the change in electron density of a molecule at a given position.

$$f(r) = \frac{\partial \rho(r)}{\partial N_{\text{electron}}} \tag{14}$$

where ρ(r) is the electron density at a position of "r" and "N" is the total number of electrons. The finite electron difference at a position (an atom) can be given by, electron gain (N + 1) and electron loss (N-1) system, Eqs. 15 and 16 respectively.

$$f^{+}(r) = q_{N+1} - q_N \tag{15}$$

$$f^{-}(r) = q_N - q_{N-1} \tag{16}$$

where f^+ (r) and f^-(r) are the condensed Fukui function for the LUMO (electrophilic) and HOMO (nucleophilic), respectively. The calculated Fukui function is presented in Table S1. As shown in Table S1, the highest electrophilic Fukui function (f^+) is located in the sulfonium sulfur S(20) while the nucleophilic function (f^-) observed at C(27) and N (21). Therefore, the adsorption of MB dye onto the zeolite 4A surface is preferentially made interaction through the sulfonium sulfur. Such interaction is further supported by the frequency analysis of each representative zeolite structure and MB-zeolite 4A (Fig. S3). The Fukui function analysis, HOMO-LUMO diagram, and frequency analysis agree with each other.

4 Conclusions

In conclusion, highly crystalline and pure phase zeolite 4A with a cubic morphology was prepared from Ethiopian kaolin using a facile low-pressure hydrothermal method. The adsorptive efficiency of zeolite 4A towards MB dye from aqueous solution studied at varying pH, zeolite 4A dose (mg), contact time (min) and concentrations of MB (mg/L). The adsorption efficiency of zeolite 4A was found to be maximum in a basic solution above the pH_{PZC} (6.86). Statistical optimization of adsorption factors such as zeolite dose, contact time and concentrations of MB, at fixed pH = 8 and temperature (25 °C) was found to be a well-fitted BBD model. The high regression

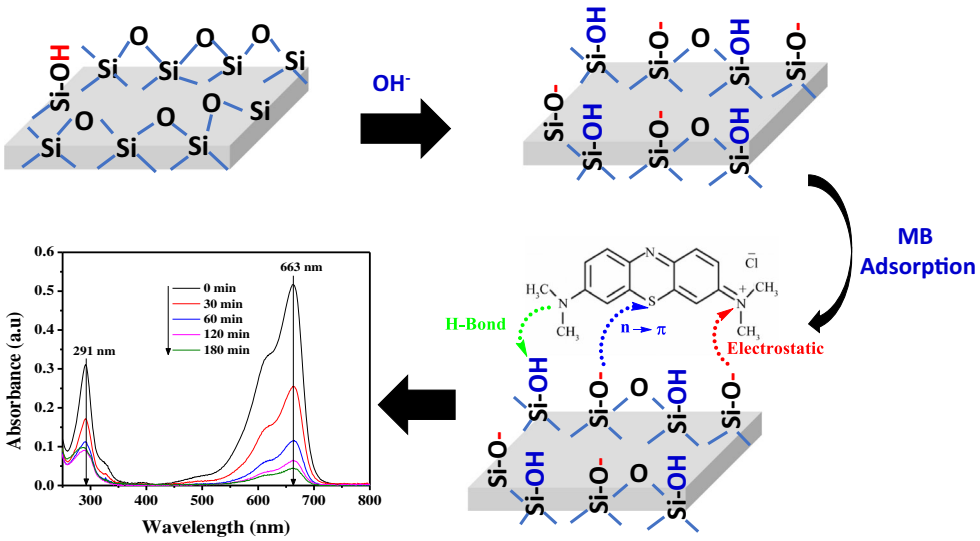

Fig. 10 The plausible adsorption mechanism of MB onto zeolite 4A in the alkali solution

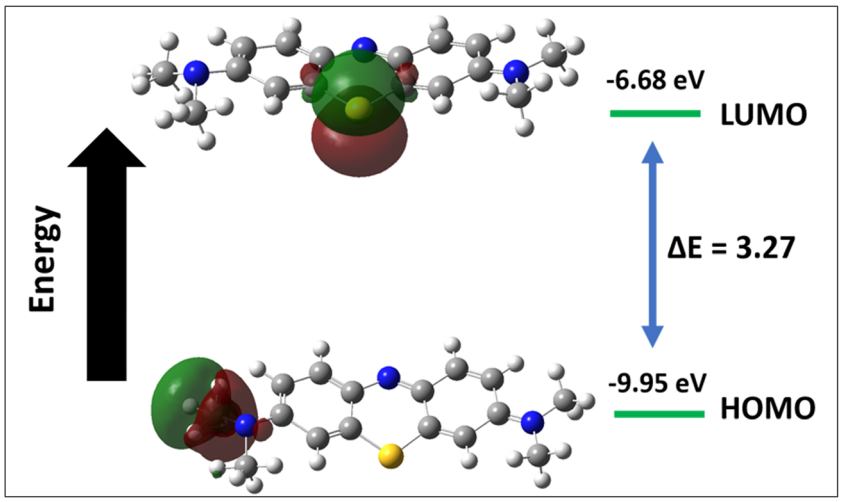

Fig. 11 The HOMO-LUMO structure of MB

($R^2 = 0.9947$) and the low probability (p value <0.0001) values signify the validity of the quadratic model to predict the removal (%) of MB. The maximum adsorptive removal of MB was found to be 99.37% at the optimum combination of 10 mg/L of MB, 39.05 mg zeolite 4A, and 179.82 contact time (min). The kinetics and isotherm of the adsorption study confirm pseudo-second-order and Langmuir isotherm are the best-fitted models for the experimental data. Kinetics study investigates 180 min as the equilibrium adsorption time. The maximum adsorption capacity (Q_{max}) was 44.35 mg g^{-1} from the Langmuir isotherm model. The mechanism of MB adsorption onto zeolite 4A is governed by the hydrogen bond, dative bond, and electrostatic interaction forces.

Supplementary Information The online version contains supplementary material available at https://doi.org/10.1007/s12633-020-00938-9.

Acknowledgments The authors grateful to Debre Berhan University and the Ministry of Education of Ethiopia for supporting the work.

Authors Contributions **Neway Belachew** works for**:** Conceptualization, Formal analysis, Methodology, Investigation, writing - original draft, and writing - review & editing. **Hirpo Hinsene** works for: Formal analysis and writing - review & editing.

Funding Not applicable.

Data Availability All data generated or analysed during this study are included in this published article.

Compliance with Ethical Standards

Competing Interests The authors declare that they have no competing interests.

Ethical Approval Not applicable.

Consent to Participate Not applicable.

Consent to Publish Not applicable.

References

1. Lellis B, Fávaro-Polonio CZ, Pamphile JA, Polonio JC (2019) Effects of textile dyes on health and the environment and bioremediation potential of living organisms. Biotechnol Res Innov 3:275–290
2. Khatri J, Nidheesh PV, Anantha Singh TS, Suresh Kumar M (2018) Advanced oxidation processes based on zero-valent aluminium for treating textile wastewater. Chem Eng J 348:67–73
3. Chung K-T (2016) Azo dyes and human health: a review. J Environ Sci Health Part C 34:233–261
4. Brown MA, De Vito SC (1993) Predicting azo dye toxicity. Crit Rev Environ Sci Technol 23:249–324
5. Geçgel Ü, Kocabıyık B, Üner O (2015) Adsorptive Removal of Methylene Blue from Aqueous Solution by the Activated Carbon Obtained from the Fruit of Catalpa bignonioides. Water, Air, & Soil Pollution 226
6. Belachew N, Kahsay MH, Tadesse A, Basavaiah K (2020) Green synthesis of reduced graphene oxide grafted Ag/ZnO for photocatalytic abatement of methylene blue and antibacterial activities. J Environ Chem Eng 8:104106
7. Rafatullah M, Sulaiman O, Hashim R, Ahmad A (2010) Adsorption of methylene blue on low-cost adsorbents: a review. J Hazard Mater 177:70–80
8. Pathania D, Sharma S, Singh P (2017) Removal of methylene blue by adsorption onto activated carbon developed from Ficus carica bast. Arab J Chem 10:S1445–S1451
9. Anwer H, Mahmood A, Lee J, Kim KH, Park JW, Yip ACK (2019) Photocatalysts for degradation of dyes in industrial effluents: opportunities and challenges. Nano Res 12:955–972
10. Kasperchik VP, Yaskevich AL, Bil'dyukevich AV (2012) Wastewater treatment for removal of dyes by coagulation and membrane processes. Pet Chem 52:545–556
11. Thamaraiselvan C, Noel M (2015) Membrane processes for dye wastewater treatment: recent Progress in fouling control. Crit Rev Environ Sci Technol 45:1007–1040
12. Bhatia D, Sharma NR, Singh J, Kanwar RS (2017) Biological methods for textile dye removal from wastewater: a review. Crit Rev Environ Sci Technol 47:1836–1876
13. Belachew N, Rama Devi D, Basavaiah K (2016) Facile green synthesis of l-methionine capped magnetite nanoparticles for adsorption of pollutant Rhodamine B. J Mol Liq 224:713–720
14. Du F, Sun L, Huang Z et al (2020) Electrospun reduced graphene oxide/TiO2/poly(acrylonitrile-co-maleic acid) composite

nanofibers for efficient adsorption and photocatalytic removal of malachite green and leucomalachite green. Chemosphere 239: 124764
15. Yagub MT, Sen TK, Afroze S, Ang HM (2014) Dye and its removal from aqueous solution by adsorption: a review. Adv Colloid Interf Sci 209:172–184
16. Raval NP, Shah PU, Shah NK (2017) Malachite green "a cationic dye" and its removal from aqueous solution by adsorption. Appl Water Sci 7:3407–3445
17. Garcia RM, Machado Garcia R, Carleer R, et al (2020) Adsorption of Cibacron yellow F-4G dye onto activated carbons obtained from peanut hull and rice husk: kinetics and equilibrium studies. Biomass Conversion and Biorefinery
18. Hameed KS, Shahul Hameed K, Muthirulan P, Meenakshi Sundaram M (2017) Adsorption of chromotrope dye onto activated carbons obtained from the seeds of various plants: equilibrium and kinetics studies. Arab J Chem 10:S2225–S2233
19. Druzian SP, Zanatta NP, Côrtes LN, Streit AFM, Dotto GL (2019) Preparation of chitin nanowhiskers and its application for crystal violet dye removal from wastewaters. Environ Sci Pollut Res Int 26: 28548–28557
20. Zhang L, Sellaoui L, Franco D, Dotto GL, Bajahzar A, Belmabrouk H, Bonilla-Petriciolet A, Oliveira MLS, Li Z (2020) Adsorption of dyes brilliant blue, sunset yellow and tartrazine from aqueous solution on chitosan: analytical interpretation via multilayer statistical physics model. Chem Eng J 382:122952
21. Tahir SS, Rauf N (2006) Removal of a cationic dye from aqueous solutions by adsorption onto bentonite clay. Chemosphere 63: 1842–1848
22. Sarma GK, Sen Gupta S, Bhattacharyya KG (2019) Removal of hazardous basic dyes from aqueous solution by adsorption onto kaolinite and acid-treated kaolinite: kinetics, isotherm and mechanistic study. SN Applied Sciences 1
23. Deng L, Shi Z, Luo L, Chen SY, Yang LF, Yang XZ, Liu LS (2014) Adsorption of hexavalent chromium onto kaolin clay based adsorbent. J Cent South Univ 21:3918–3926
24. Boukhemkhem A, Rida K (2017) Improvement adsorption capacity of methylene blue onto modified Tamazert kaolin. Adsorption Sci Technol 35:753–773
25. Nandi BK, Goswami A, Das AK, Mondal B, Purkait MK (2008) Kinetic and equilibrium studies on the adsorption of crystal violet dye using kaolin as an adsorbent. Sep Sci Technol 43:1382–1403
26. Zen S, El Berrichi FZ (2016) Adsorption of tannery anionic dyes by modified kaolin from aqueous solution. Desalin Water Treat 57: 6024–6032
27. Han H, Rafiq MK, Zhou T, Xu R, Mašek O, Li X (2019) A critical review of clay-based composites with enhanced adsorption performance for metal and organic pollutants. J Hazard Mater 369:780–796
28. Belachew N, Hinsene H (2020) Preparation of cationic surfactant-modified kaolin for enhanced adsorption of hexavalent chromium from aqueous solution. Appl Water Sci 10:38
29. Belver C, Muñoz MAB, Vicente MA (2002) Chemical activation of a kaolinite under acid and alkaline conditions. Chem Mater 14: 2033–2043
30. Magdy A, Fouad YO, Abdel-Aziz MH, Konsowa AH (2017) Synthesis and characterization of Fe 3 O 4 /kaolin magnetic nanocomposite and its application in wastewater treatment. J Ind Eng Chem 56:299–311
31. Frost RL, Makó É, Kristóf J, Horváth E, Kloprogge JT (2001) Modification of kaolinite surfaces by Mechanochemical treatment. Langmuir 17:4731–4738
32. Ayele L, Pérez-Pariente J, Chebude Y, Díaz I (2015) Synthesis of zeolite a from Ethiopian kaolin. Microporous Mesoporous Mater 215:29–36
33. Ayele L, Pérez E, Mayoral Á, Chebude Y, Díaz I (2018) Synthesis of zeolite a using raw kaolin from Ethiopia and its application in removal of Cr(III) from tannery wastewater. J Chem Technol Biotechnol 93:146–154
34. Johnson EBG, Arshad SE, Asik J (2014) Hydrothermal synthesis of zeolite a using natural kaolin from KG. Gading Bongawan Sabah. J Appl Sci 14:3282–3287
35. Wang P, Sun Q, Zhang Y, Cao J (2019) Synthesis of zeolite 4A from kaolin and its adsorption equilibrium of carbon dioxide. Materials 12. https://doi.org/10.3390/ma12091536
36. Hildebrando EA, Andrade CGB, da Rocha Junior CAF et al (2014) Synthesis and characterization of zeolite NaP using kaolin waste as a source of silicon and aluminum. Mater Res 17:174–179
37. Caballero I, Colina FG, Costa J (2007) Synthesis of X-type zeolite from Dealuminated kaolin by reaction with sulfuric acid at high temperature. Ind Eng Chem Res 46:1029–1038
38. Kovo AS, Holmes SM (2010) Effect of aging on the synthesis of kaolin-based zeolite Y from Ahoko Nigeria using a novel Metakaolinization technique. J Dispers Sci Technol 31:442–448
39. Arshad SE, Yusslee EF, Rahman ML, et al (2017) Hydrothermal synthesis of free-template zeolite T from kaolin
40. Wang P, Sun Q, Zhang Y, Cao J (2019) One-step hydrothermal synthesis of zeolite KA from kaolin. Micro Nano Lett 14:1298–1302
41. Mackinnon IDR, Millar GJ, Stolz W (2012) Hydrothermal syntheses of zeolite N from kaolin. Appl Clay Sci 58:1–7
42. Kovo AS, Hernandez O, Holmes SM (2009) Synthesis and characterization of zeolite Y and ZSM-5 from Nigerian Ahoko kaolin using a novel, lower temperature, metakaolinization technique. J Mater Chem 19:6207
43. Eiad-ua A, Amnaphiang P, Asawaworarit P, et al (2018) Zeolite P from kaolin via hydrothermal method
44. Ugal JR, Hassan KH, Ali IH (2010) Preparation of type 4A zeolite from Iraqi kaolin: characterization and properties measurements. J Assoc Arab Univ Basic Appl Sci 9:2–5
45. Li W, Yan C, Hu W (2010) Synthesis and characterization of zeolite 4A from soft kaolin. Desalin Water Treat 22:87–90
46. Chandrasekhar S (1996) Influence of metakaolinization temperature on the formation of zeolite 4A from kaolin. Clay Miner 31: 253–261
47. Du C, Yang H (2010) Synthesis and characterization of zeolite 4A-type desiccant from kaolin. Am Mineral 95:741–746
48. Fabbri B, Gualtieri S, Leonardi C (2013) Modifications induced by the thermal treatment of kaolin and determination of reactivity of metakaolin. Appl Clay Sci 73:2–10
49. Miao Q, Zhou Z, Yang J, Lu J, Yan S, Wang J (2009) Synthesis of NaA zeolite from kaolin source. Front Chem Eng China 3:8–11
50. Bish DL (1989) Rietveld refinement of non-hydrogen atomic positions in kaolinite. Clay Clay Miner 37:289–296
51. Zavareh S, Farrokhzad Z, Darvishi F (2018) Modification of zeolite 4A for use as an adsorbent for glyphosate and as an antibacterial agent for water. Ecotoxicol Environ Saf 155:1–8
52. Tironi A, Trezza MA, Irassar EF, Scian AN (2012) Thermal treatment of kaolin: effect on the Pozzolanic activity. Procedia Mater Sci 1:343–350
53. Nakamoto K (2008) Infrared and Raman Spectra of Inorganic and Coordination Compounds, Part A and Part B, 2 Volume Set. Wiley-Interscience
54. Murali RS, Surya Murali R, Ismail AF et al (2014) Mixed matrix membranes of Pebax-1657 loaded with 4A zeolite for gaseous separations. Sep Purif Technol 129:1–8
55. Zou W, Bai H, Zhao L, Li K, Han R (2011) Characterization and properties of zeolite as adsorbent for removal of uranium(VI) from solution in fixed bed column. J Radioanal Nucl Chem 288:779–788
56. Dahani W, Subandrio S, Marwanza I, et al (2020) Direct transformation of Bangka kaolin to zeolite 4A: Effect of hydrothermal

temperature. 3RD International postgraduate conference on materials, minerals & polymer (MAMIP) 2019
57. Cobas M, Sanromán MA, Pazos M (2014) Box–Behnken methodology for Cr (VI) and leather dyes removal by an eco-friendly biosorbent: F. vesiculosus. Bioresour Technol 160:166–174
58. Trinh H, Yusup S, Uemura Y (2018) Optimization and kinetic study of ultrasonic assisted esterification process from rubber seed oil. Bioresour Technol 247:51–57
59. Belachew N, Bekele G (2020) Synergy of magnetite intercalated Bentonite for enhanced adsorption of Congo red dye. Silicon 12: 603–612
60. Cimirro NFGM, Lima EC, Cunha MR, Dias SLP, Thue PS, Mazzocato AC, Dotto GL, Gelesky MA, Pavan FA (2020) Removal of pharmaceutical compounds from aqueous solution by novel activated carbon synthesized from lovegrass (Poaceae). Environ Sci Pollut Res Int 27:21442–21454
61. Mukherjee K, Kedia A, Jagajjanani Rao K, Dhir S, Paria S (2015) Adsorption enhancement of methylene blue dye at kaolinite clay–water interface influenced by electrolyte solutions. RSC Adv 5: 30654–30659
62. Ameh PO, Eddy NO (2016) Theoretical and experimental studies on the corrosion inhibition potentials of 3-nitrobenzoic acid for mild steel in 0.1 M H2SO4. Cogent Chemistry 2
63. Odoemelam SA, Emeh UN, Eddy NO (2018) Experimental and computational chemistry studies on the removal of methylene blue and malachite green dyes from aqueous solution by neem (Azadirachta indica) leaves. J Taibah Univ Sci 12:255–265